

Article

# Structural Control of a Dissolution Network in a Limestone Reservoir Forced by Radial Injection of CO<sub>2</sub> Saturated Solution: Experimental Results Coupled with X-ray Computed Tomography

Vitaliy Privalov \*, Aurélien Randi \*, Jérôme Sterpenich , Jacques Pironon  and Christophe Morlot

GeoRessources UMR7359 CNRS, Université de Lorraine-CREGU, BP70239 Vandoeuvre-les-Nancy, France; jerome.sterpenich@univ-lorraine.fr (J.S.); jacques.pironon@univ-lorraine.fr (J.P.); christophe.morlot@univ-lorraine.fr (C.M.)

\* Correspondence: vitaliy.privalov@gmail.com (V.P.); aurelien.randi@univ-lorraine.fr (A.R.)

Received: 9 October 2018; Accepted: 28 December 2018; Published: 9 January 2019



**Abstract:** This study was conducted in the framework of the PILOT CO<sub>2</sub>-DISSOLVED project, which provides an additional approach for CO<sub>2</sub> sequestration, with the aims of capturing, injecting, and locally storing the CO<sub>2</sub> after being dissolved in brine. The brine acidity is expected to induce chemical reactions with the mineral phase of the host reservoir. A set of continuous radial CO<sub>2</sub> flow experiments was performed on cylindrical carbonate rock samples under geological storage conditions. The objective was to interpret the dissolution network morphology and orientation involved. To explore the three-dimensional architecture of dissolution arrays and their connection integrity within core samples, we used computed tomography. A structural investigation at different scales revealed the impact of the rock heterogeneity on the dissolution pathways. The initial strike of the observed mesoscopic wormholes appears to be parallel to dilatational fractures, with a subsequent change in major trends of dissolution along master shears or, more specifically, a combination of synthetic shears and secondary synthetic shears. Antithetic shears organize themselves as slickolitic surfaces, which may be fluid-flow barriers due to different mineralogy, thus affecting the permeability distribution-wormhole growth geometry induced by CO<sub>2</sub>-rich solutions.

**Keywords:** CO<sub>2</sub>-rich aqueous solution; radial injection; dissolution array; X-ray computed tomography; morphology of wormhole; regional strike-slip zone; Riedel shears; artificial karstification pattern

## 1. Introduction

Capture, transport, and subsequent injection of anthropogenic CO<sub>2</sub> into deep geological horizons of highly-permeable sedimentary rocks effectively reduces atmospheric emissions of CO<sub>2</sub> derived from the combustion of fossil fuels. The injection of CO<sub>2</sub> into deep geological formations uses technologies that have been traditionally applied and verified by the oil and gas industry. However, validating potential storage reservoirs from the standpoint of environmental risks, which may arise from uncertainties in geometrical characteristics of leakage pathways from injection wells into adjoining stratigraphic intervals, is crucial. Leakage of CO<sub>2</sub> could have various impacts, including contamination of groundwater, which affects local health and safety.

Considerable attention has been paid to the suitability of horizons at depths of approximately 1500 m in the central part of the Paris Basin (France) for supercritical CO<sub>2</sub> storage installation. These include 70–80-m-thick oolitic carbonate horizon from the Dogger and uppermost carbonate

formation of Oolite Blanche Series [1,2], which lie directly beneath impermeable argillaceous rocks of Callovian–Oxfordian age. The Oolite Blanche Series can be observed in outcrops at the basin edges, wherein these limestones have been extensively excavated (e.g., in the vicinity of Poitiers and Chauvigny, where Lavoux limestone is still being quarried). This formation serves as an aquifer with moderate salinity that has been used for geothermal projects for more than 40 years.

In accordance with previous experiments [3–5], the reactivity of Lavoux limestone (mainly composed of calcite) is sensitive to pH and, therefore, to the partial pressure (P) of CO<sub>2</sub> in the interstitial solution. Thermodynamic calculations [4] have demonstrated that the volume of dissolved calcite is obviously limited by storage conditions due to the H<sub>2</sub>O–CO<sub>2</sub>–calcite equilibrium in closed systems. However, these limitations occur at some edges of the dissolution front away from the injection well, where CO<sub>2</sub> is transported along attractive planes of diffusion. Rahbari and Saberi [6] introduced a mathematical model of the growth of this three-dimensional (3D) pattern, where diffusion process, as a 3D Brownian motion, was controlled by the attractive planes. Owing to the complex internal geometry of solute flow paths, including sink conduits and blind pockets, we can expect significant local, real-time deviations of pH–P conditions, which are responsible for dissolution and contemporaneous re-precipitation in some domains of the host rock. According to Fischer and Lüttge [7], the heterogeneity of polycrystalline calcite causes a pattern of fluid flow velocity gradients that retroact on surface dissolution rates. Direct observations using atomic force microscopy, optical interferometry, surface spectroscopy, and related instrumental approaches have provided significant advancements in our understanding of mineral dissolution, in which kinetics are typically dominated by the distribution of defects and defect-driven reactions [8], which may constitute a critical contribution to whole rock reactivity.

Since 2012, the French National Research Agency (ANR) launched the CO<sub>2</sub> DISSOLVED research project [9,10], employing the Carbon Capture and Storage (CCS) concept based on environmentally-friendly technology integrating a geothermal doublet system consisting of two wells targeted for a deep saline aquifer in a carbonate reservoir. The first injection well is used for injecting and storing CO<sub>2</sub> in dissolved form produced by low tonnage emitters, whereas the second production well is employed for simultaneous geothermal energy recovery. This study was conducted in the framework of the PILOT CO<sub>2</sub>-DISSOLVED project (funded by the Scientific Interest Group Geodenergies) with the ultimate aim of careful site selection for understanding the geometrical characteristics of possible CO<sub>2</sub> leakage pathways from the injection well during implementation of the forthcoming industrial pilot demonstration project. For this purpose, a test bench (MIRAGES-2), mimicking an injection well at a 1/20 scale (rock/cement/tubing), was developed by the GeoResources Laboratory to allow the continuous radial injection of a CO<sub>2</sub>-rich aqueous solution under geological storage conditions.

The characteristics of the dissolution network within reservoir rocks were produced by CO<sub>2</sub>-like and more complex fluid-carbonate rock alterations. These are critical for defining possible injection scenarios for feasibility studies related to installation and safe, long-term exploitation of a CCS industrial pilot demonstration project.

## 2. Investigation and Methodology of MIRAGES-2 Experiments

### 2.1. Experimental Protocol

The MIRAGES devices were initially designed by GeoResources Laboratory (Nancy, France) to validate the numerical simulations of modes of behavior and the interaction of casing materials (steel, composite materials) with reservoir rocks, including estimation of induced corrosion effects during and after injection of supercritical CO<sub>2</sub> under geological conditions of pressure and temperature. A detailed depiction of MIRAGES experimental devices was provided by Sterpenich et al. [11].

The main objective of a series of new experiments using the MIRAGES-2 [12] device was to obtain a physical and chemical model of the formation of the dissolution arrays linked to the injection of

aggressive fluids of different compositions under realistic temperature-pressure storage conditions occurring in the Dogger formation of the Paris basin at a 1500 m depth.

A set of 8 experiments was performed on cylindrical samples of the Lavoux limestone extracted from monolithic bulk samples quarried at the subsurface level from Chauvigny within the Vienne River valley (France).

The samples of limestones (Figure 1b) were inserted into a batch reactor made of stainless steel 316SS with a triple Teflon (MAXIMATOR® France, Rantigny, France) coating on the wall of the vessel and the cover lid to avoid corrosion problems (CO<sub>2</sub> + NaCl), which was connected to a coupled system composed by a dual syringe pump (A500 Teledyn ISCO, Lincoln, NE, USA) and liquid mass Coriolis flow meter (Bronkhorst®, Montigny-Les-Cormeilles, France) allowing a continuous and constant injection of aqueous solutions in the core-plug containing dissolved CO<sub>2</sub> and with or without salt (Figure 1a).

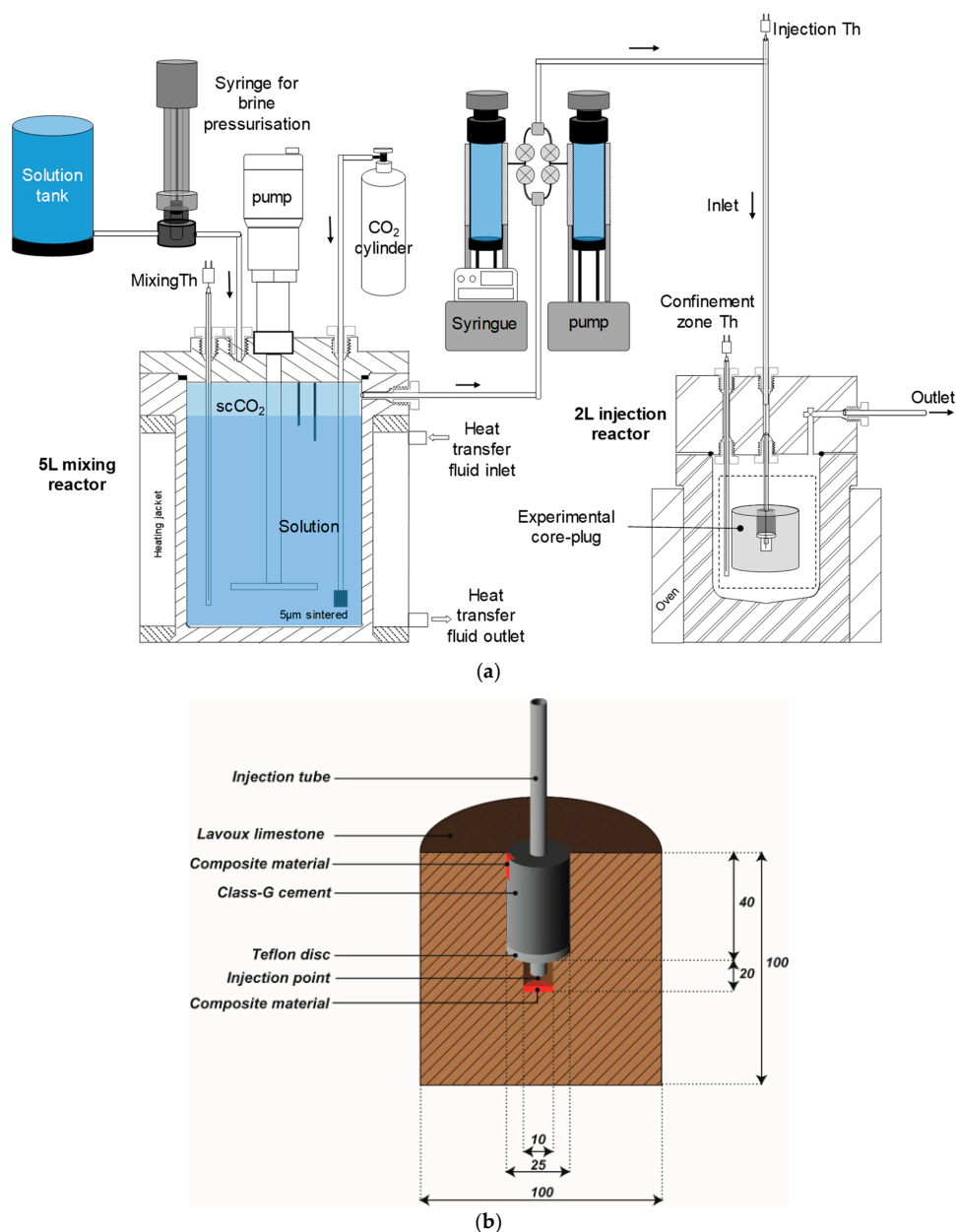


**Figure 1.** (a) Experimental device (MIRAGES-2) used to inject the CO<sub>2</sub>-rich solution in the core-plug under controlled conditions of pressure, temperature, and flow rate; (b) schematic view of the core-plug and the injection well. Dimensions are provided in millimetres.

Core-plugs were forced into the MIRAGES-2 device for different regimes of treatments with injections of specific fluids: Pure water with atmospheric CO<sub>2</sub> presence (experiment #1), short-term (experiments #2, #6, and #9), and long-term (experiments #3 and #7) with CO<sub>2</sub>-dissolved fluids and CO<sub>2</sub>-rich saline fluid (experiments #4 and #8; 15 g/L NaCl). All experiments were conducted under thermodynamic conditions similar to real reservoir simulation parameters (e.g., pressure P = 120 bar, temperature T = 60 °C) with a constant rate of fluid injection (150 g/h). All experiments except experiment #1 were performed with dissolved CaCO<sub>3</sub> (15 mg/kg) to limit the initial dissolution of the core-plug during the cure period. Refer to previous studies [12,13] for a complete description of the experiment.

Experiment #7 (9.8 days of forced injection into sample equilibrated water with 15 mg of CaCO<sub>3</sub>/kg of solution and 0.929 mole/kg of CO<sub>2</sub>) was carried out for imitation of the real inclination of an injection well (55°) proposed for the pilot project. The conditions of the 8 performed experiments are summarised in Table 1.

**Table 1.** Summary of the conditions for the performed experiments.

Experiment No./X-ray CT Resolution	Drilling Inclination	Composition of Fluid Injected with Permanent Flow Rate 150 g/h	Time of Curing <sup>1</sup> (Days)	Time of Ageing <sup>2</sup> (Days)	Volume of Injected Fluid (L)
#1/100 μm	⊥	pure water at equilibrium with atmospheric CO <sub>2</sub> = 0.0372 mole/kg	9.10	21.00	71.18
#2/60 μm	⊥	water + 15 mg/L CaCO <sub>3</sub> + dissolved CO <sub>2</sub> (CO <sub>2</sub> solubility of the injected solution = 0.94 mole/kg)	10.27	2.58	10.32
#3/60 μm	⊥	water + 15 mg/L CaCO <sub>3</sub> + dissolved CO <sub>2</sub> (CO <sub>2</sub> solubility of the injected solution = 0.94 mole/kg)	9.90	20.90	73.70
#4/60 μm	⊥	water + 30 mg/L CaCO <sub>3</sub> + 15 g/L NaCl + dissolved CO <sub>2</sub> (CO <sub>2</sub> solubility of the injected solution = 0.89 mole/kg)	9.78	21.16	74.32
#6/52 μm	⊥	water + 15 mg/L CaCO <sub>3</sub> + dissolved CO <sub>2</sub> (CO <sub>2</sub> solubility of the injected solution = 1.01 mole/kg)	10.77	0.99	3.49
#7/52 μm	#55°	water + 15 mg/L CaCO <sub>3</sub> + dissolved CO <sub>2</sub> (CO <sub>2</sub> solubility of the injected solution = 0.93 mole/kg)	9.80	9.95	35.15
#8/52 μm	⊥	water + 30 mg/L CaCO <sub>3</sub> + 15 g/L NaCl + dissolved CO <sub>2</sub> (CO <sub>2</sub> solubility of the injected solution = 0.88 mole/kg)	10.02	7.93	27.89
#9/52 μm	⊥	water + 15 mg/L CaCO <sub>3</sub> + dissolved CO <sub>2</sub> (CO <sub>2</sub> solubility of the injected solution = 0.96 mole/kg)	10.37	0.52	2.00

⊥ Cores were drilled perpendicularly to the bedding. <sup>1</sup> Time of subjecting sample to the reservoir thermodynamic conditions in a close system. <sup>2</sup> Time of fluid injection under reservoir conditions.

## 2.2. X-ray Computed Tomography and Scanning Electron Microscopy

To explore the 3D architecture of dissolution arrays and their connection integrity within core samples, we performed computed tomography (CT) using the X-ray Nanotom Phoenix GE system (GE Inspection Technologies<sup>®</sup>, Limonest, France) at the GeoResources Laboratory, with resolutions varying from 52 μm to 100 μm/voxel. X-ray CT is a non-destructive technique of assessing the density-dependant internal structure of a solid specimen by recording the attenuations of the levels of X-rays after passing through the sample.

The studied samples were illuminated by an X-ray beam with a constant adjustment 145 Kv 300 μm X-ray generator. The dissolution patterns in the internal structure of studied samples were

recorded on a 5 Mpx flat panel sensor as a set of radiographic images. The tomography collected 1500 viewing angles (1 radiography by 0.24 degree) for reconstructing the 3D models.

For digital geometry processing and the following 3D visualization, exploration, and quantification analysis of dissolution patterns, VGStudio 2.2 (Volume Graphics, Heidelberg, Germany) and Avizo 9.2 (ThermoFischer Scientific, Hillsbro, OR, USA) software packages were used.

The scanning electron microscope, TESCAN VEGA3 (TESCAN, Brno-Kohoutovice, Czech Republic), equipped with an energy dispersive X-ray (EDS) detector, was used for microstructural and chemical characterisation of selected fracture surfaces.

### 3. Experimental Results

Matrix acidizing of the carbonate rocks was triggered by the injection of aggressive fluids in a set of eight different experiments. These experiments generated sets of dissolution arrays, which appeared to be due not only to continuous uniform alteration or the stochastic branch working in porous limestone medium, but also to the physical and chemical competition between enlarging unitary flow paths and tectonically-induced conduits and barriers, involving both fluid-reservoir rock dissolution and precipitation interactions.

#### 3.1. Reactivity of Lavoux Limestone after Computed Tomography Inspection

The injection of aggressive fluids promoted dissolution of the limestone in the studied samples from the injection point to the exterior of the samples. After CT inspection, the core plugs demonstrated dissolution networks visible on the CT scans and 3D models (Figure 2).

Notably, prominent anisotropy of the multilevel dissolution pathways was observed, whereas the injection process was basically isotropic from the bottom hole. This strongly suggests the presence of an initial anisotropy in the samples of the Lavoux formation even before experimental treatment. Despite the dramatic differences in the initial experimental conditions, including the duration of the treatment under reservoir conditions and different compositions of injected fluids, the results identify recurrent directional control of patterns in each dataset. It appears that the similarity of the dissolution pathways repeated in all experiments must be more than a coincidence. Specifically, the experiments demonstrated that preferential directions “attracted” dissolution and resulted in systems of highly conductive channels, referred to as wormholes. Especially prominent, similar patterns in the dissolution arrays can be seen by comparison of the CT scans with related 3D models in pairs of experiments (#1, #2, #3, and #4) presented in Figure 2.

Prior to the experiments, we considered the existence of pre-existing fabrics and related preferential directions that were pronounced in the samples. These directions could facilitate wormhole propagation and the overall growth of the entire dissolution pattern.

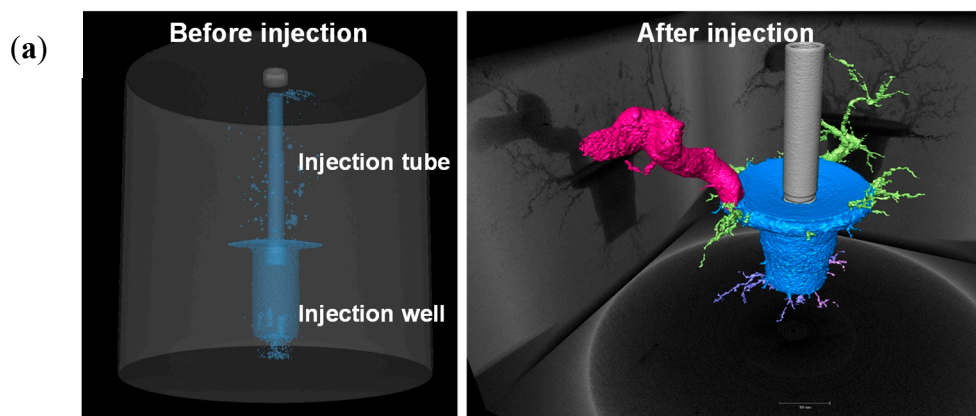
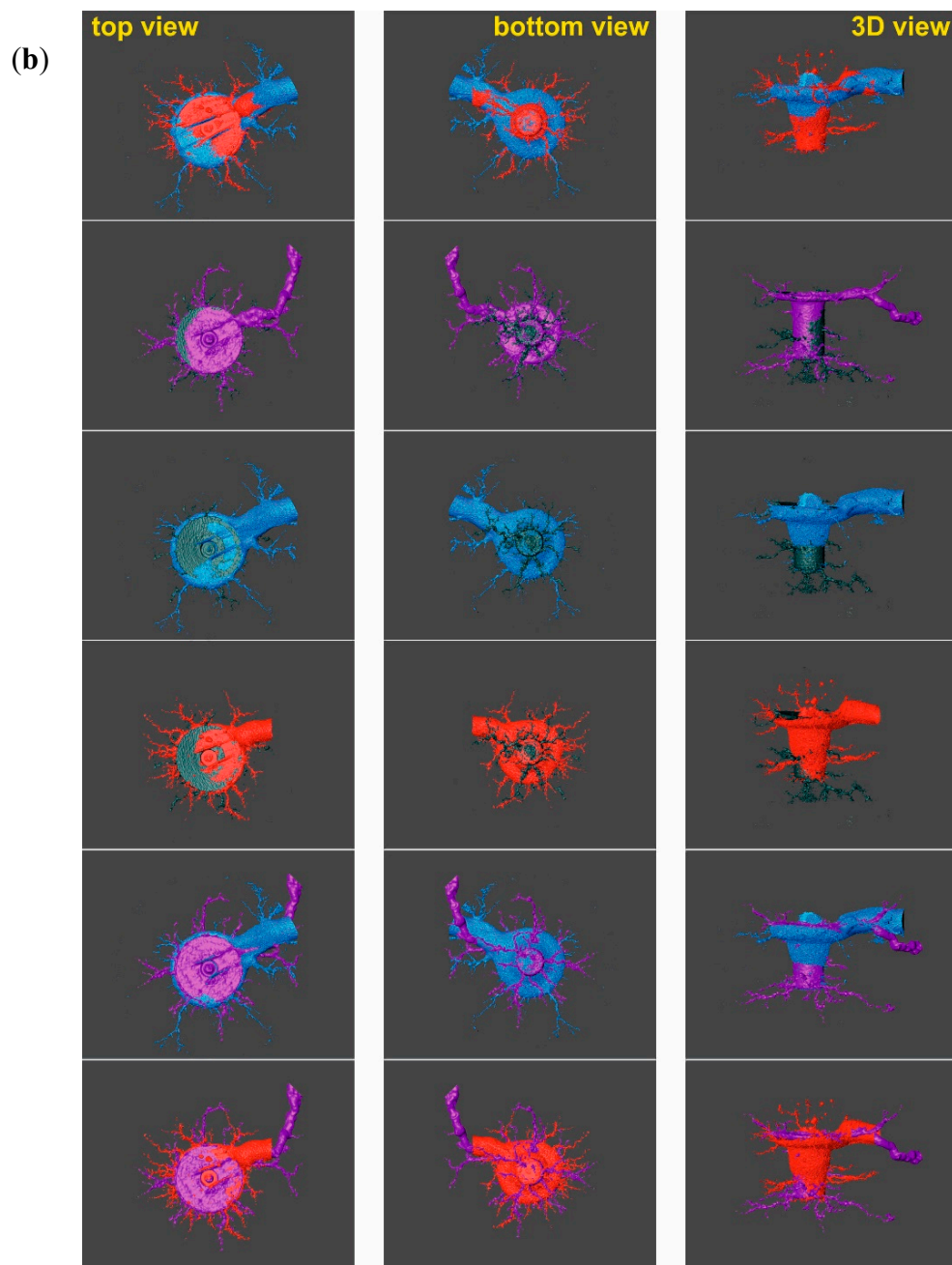


Figure 2. Cont.



**Figure 2.** (a) Computed Tomography (CT) scan of injection well vicinity before and after injection of CO<sub>2</sub>-rich solution. Notice the development of a dissolution network with one dominant wormhole (pink) after 10 days of injection; (b) comparison of obtained dissolution arrays (top views, bottom views, and 3D models) based on CT scan results in pairs of experiments. Different colors correspond to the experiment number: Grey is #1, purple is #2, red is #3, and blue is #4. Vertical columns of images correspond to: **Left**–top view in horizontal plane; **middle**–bottom view in horizontal plane; **right**–side 3D view in vertical plane.

### 3.2. Similarities of Subsequent Dissolution Development in Natural Environments and Artificial Wormhole Propagation from the Standpoint of the Influence of Pre-Existing Structural Discontinuities

Researchers have been looking for the mechanism for wormhole formation and various models to describe this process have been proposed [14–19]. However, there is still no consensus on global wormhole theory. Most of the traditional models [14] advocate the hypothetical random distribution

of pores in the shape of cylindrical tubes, with their enlargement being a response to aggressive fluid injection.

Experimental studies of wormhole formation have used a variety of porous systems, including plaster dissolved by water [15], limestone cores treated with acid [16], and salt packs dissolved with under-saturated salt solution [17]. Multiple types of dissolution networks along discrete rock fractures and their zones have been reported [17–19]. This approach to wormhole distribution analysis resembles the conduit initiation and growth of cavities in a karst system, and can be referred to as the principal mechanism of a preferable dissolution pattern nucleation developed along zones of structural weakness represented by faults and fractures of different scales.

The high-permeability subsurface horizons are typically derived from biological and igneous processes and chemical reactions between rocks and fluids, including greenhouse gases, such as carbon dioxide. In sedimentary basins, natural accumulations of relatively pure CO<sub>2</sub> and CO<sub>2</sub> dissolved in formation waters have been found in a number of different types of sedimentary rocks, especially in limestones, dolomites, and sandstones, with a variety of seals and a range of trap types, reservoir depths, and CO<sub>2</sub>-bearing phases. Geological storage of CO<sub>2</sub> dissolved in formation waters occurred as a natural process in carbonate rocks (e.g., limestones) for millions of years and this natural laboratory provides a basis for understanding possible scenarios of the behavior of industrial CO<sub>2</sub> storage in carbonate lithology formations.

More specifically, long-term natural storage of CO<sub>2</sub> in carbonate rock aquifers are most likely accompanied by artificial karstification due to acidic water-rock interactions. Conduit initiation and progressive growth of cavities in a karst system are usually assumed to be controlled by non-linear kinetics [20] that allow CO<sub>2</sub>-enriched aggressive water to penetrate geological formations. In most cases, this process mainly occurs along zones of structural weakness represented by faults and fractures on different scales [21,22].

Moreover, competition exists between conduit evolution along different fractures, and many karst corridors are closely related, not only with open tension fractures, but also with relatively tight strike-slip faults [20]. The structural network of faults and fractures, recognizable both at the surface and inside the karst systems in the transpressional structure of the Italian Dolomites, has been interpreted to be consistent with a Riedel shear system [23]. The existence of preferential orientations of conduits within karst networks has been demonstrated [24]. The structural relationship between fault families and the preferential orientation of cave survey data was identified within the Picos del Europa Mountains (Spain) [22] and a dextrally reactivated shear zone was recognized [25].

Reactions of dissolution—precipitation during experimental injection of CO<sub>2</sub> into a limestone reservoir—predominantly occur within the fractures, which serve as preferential paths for fluid flow [26]. However, the specifics of the laboratory equipment being used in this study [26] forced unidirectional transport of aggressive liquid into the specimen, with subsequent propagation of the dissolution pattern within fractures exclusively oriented along the maximal gradient of the fluid flow. This means that the effect of natural sample heterogeneity and permeability anisotropy caused by fracturing and layering on dissolution pattern structure is beyond the scope of such experiments. The ability to induce radial fluid flow in relation to an injection point is one of the major advantages offered by the MIRAGES-2 device, which ultimately helps to identify and quantify experimental results from the standpoint of understanding the spatial relation between the fracture distribution in a specimen and the subsequent dissolution development in natural environments of limestones reservoirs.

### *3.3. Structural Arrangement of Planar Microfractures in Samples of the Lavoux Limestone from X-ray Computed Tomography*

We performed a detailed examination of CT scans of fresh samples of Lavoux limestones with a 5 μm resolution in sub-horizontal sections and observed regularly arranged microscale planar fractures along which we recorded small amounts of dextral and sinistral shear displacements (Figure 3a).

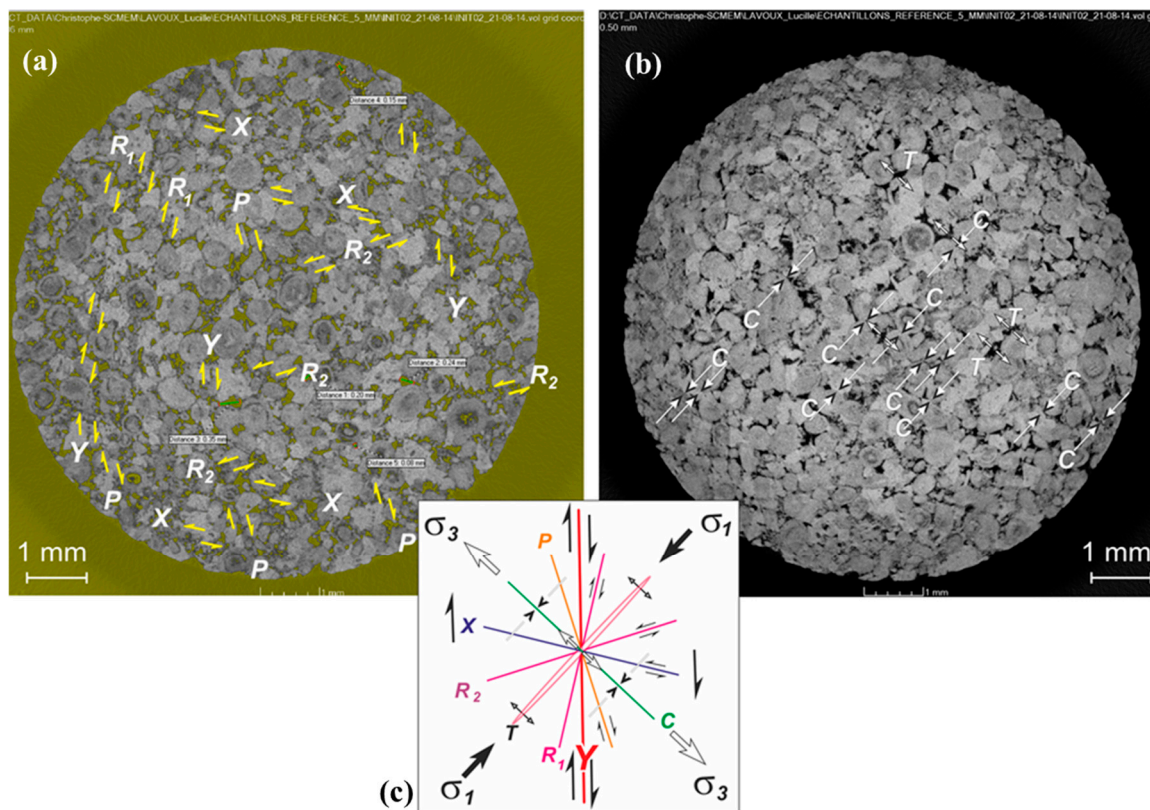


**Figure 3.** (a) CT scans of a sample of the Lavoux limestone (resolution 5  $\mu\text{m}$ ) in sub-horizontal sections with delineation within them at microscale-level planar fractures of Y,  $R_1$ ,  $R_2$ , P, and X types with identification of the direction of shear displacement (double yellow arrows); (b) stylolitic contacts of ooids C (white arrows), and dilatational joints; (c) Note, CT scans and the constructed (on the basis of interpretation of obtained kinematic types of fractures) model of formation of subsidiary fractures (modified from Hancock [27]) within dextral strike-slip zone are not azimuthally referenced.

These shear-stress-affected surfaces contain minute brecciated fragments abraded from larger ooids grooved and cracked particles. Fractures propagated mainly along ooidal grain boundaries, but also several intra-ooidal cracks with lateral shifting of grain fragments are recognised (Figure 3a). Also, tension fractures (T) or dilatational joints with no displacement parallel to the sidewalls of the fracture and tectonically-induced stylolitic contacts of ooids, as a product of intergranular pressure-solution, are visible (Figure 3b).

The presence of stylolitic planes (C) in horizontal sections is often an indication of a volume loss within the deforming material under main compressive tectonic stress ( $\sigma_1$ ) perpendicular to the stylolites. The tectonic stylolites in the WNW–ESE direction in the mid-Jurassic oolitic reservoirs in the Paris Basin were described previously by Granier and Staffelbach [28], who indicated that compressional stress ( $\sigma_1$ ) was applied from NNW–SSE directions (azimuth N150° E). Also, specific lineations, orthogonal to stylolites, have been delineated and interpreted as dilatational joints (T). Here, fracture surfaces exist normal to the main tensile stress during joint formation.

A total set of fractures identified within horizontal CT scans could be generated within the dextral strike-slip zone with the principal direction, Y, in the classical framework scheme of development of the set of subsidiary structures within the strike-slip zone [27]. These subsidiary structures consist of:

- Conjugated dextral synthetic ( $R_1$ ) and sinistral antithetic ( $R_2$ ) Riedel shears;
- conjugated dextral synthetic P and sinistral antithetic X shears; and
- stylolitic planes (C) perpendicular to the main compressive stress,  $\sigma_1$ .

- Tension fractures (dilatational joints) were T perpendicular to the main tensile stress,  $\sigma_3$ , which formed parallel to the strain ellipse short axis, C.

All these fissures or microfaults are connected to one another, forming the specific pattern of an anastomosing network of fissures (Figure 3c). Additional support for the presence within the studied samples of microcracks induced by strike slip faulting may be obtained from the analysis of the vertical sections of Lavoux limestones with the help of binary filtration of CT scans. The vertical section (Figure 4a) demonstrates the presence of both features, i.e., elements of intra-stratification and characteristic shapes of minute-scale flower structures [29], which can be interpreted as upward splaying shear microfaults. These findings are in good agreement with previously published results of geostructural surveys within the Saint-Maixent-l'École mapping sheet located in the vicinity of Chauvigny [30]. The faults inferred from the Mesozoic formations tend to join downward into single strands in the same way (Figure 4b), as we documented for high-resolution CT scans of millimeter-scale fragment of Lavoux limestone specimen.

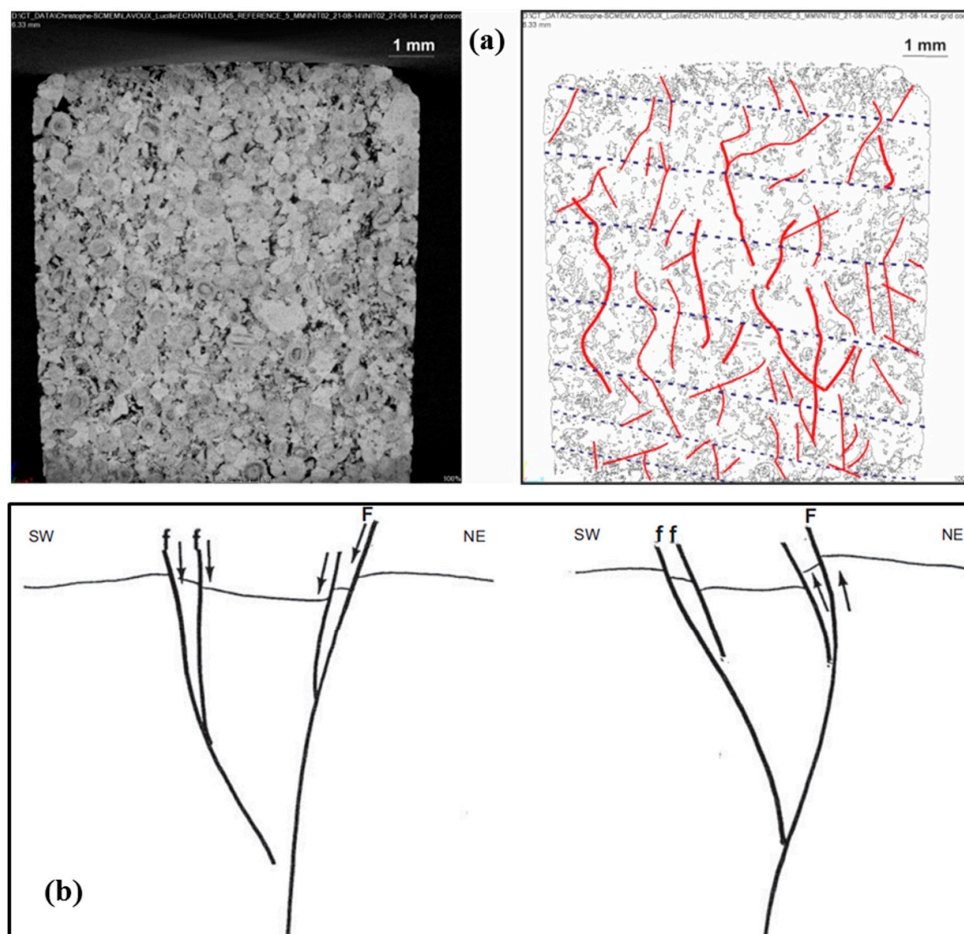


**Figure 4.** (a) CT scans of samples of Lavoux limestone in the vertical section with delineation within at the microscale-level microlayer boundaries (dashed blue lines) and upward splaying shear microfaults (red lines); (b) structural data of the Saint-Maixent-l'École graben [30]; this segment of the Southern Armorican Shear Zone is located ~80 km southwest of Chauvigny. The major faults “F” inherited the Variscan basement faults and complimentary sedimentary carapace’s antithetic faults “f” tend to join downward into single strands, forming a specific pattern of flower structures as a typical marker of lateral movements associated with strike-slip zones. Note, this structural interpretation of the regional tectonic structure of the study area (b) is compatible with our results of microfaults’ matrix interpretation (a). Note also for (b) the regional scale (several tens of km) to be compared with the centimetric scale in (a).

Here, localization of discrete microfractures corresponds to inherited mechanical anisotropy caused by millimeter-scale sedimentary layering. From our premise of preferential direction of dissolution arrays obtained within the results of MIRAGES-2, experiments should be related to precursors of brittle microcracks nucleation, resulting from the influence of the natural strike-slip stress field that affected the Lavoux limestones in-situ within the Chauvigny quarry location.

The azimuthal referencing systems of revealed microcracks in the Lavoux samples were derived using scale invariance and regional tectonic and geomorphic patterns analyses.

#### *3.4. Scale Invariance, Regional Tectonic, and Geomorphic Patterns Analyses as Tools for Azimuthal Referencing of Experimentally Obtained Dissolution Arrays and Connection with Fault and Fracture Networks at Different Scales*

The scale invariance of geological phenomena is one of the first concepts taught to students of geology [31]. Without the scale bar, it is mostly impossible to determine whether the delineated fracture pattern is a result of the interpretation of satellite imagery, aerial photographs, outcrop-scale documentation, or fault damage zone inspection after visual core observation, even if these are nano-fissure systems obtained from X-ray CT scans. There is ground truth of experimentally-derived similarities between shear zones of different magnitudes [25]. Zooming into details of arrangements of discrete brittle and semi-brittle fractures within shear zones of different scales [27,29,32] proves that there is no principal difference between processes of crustal mega-scale, local meso-scale, and even micro-scale shear zone formation in terms of the arrangement of subsidiary faults and their kinematic types.

Can we use this scale invariance phenomenon to derive a suitable solution for azimuthal referencing systems of microcracks deduced from CT scans in the samples of the Lavoux limestone? We think this is possible if we consider the information about trends of tectonic structures, topography, and drainage patterns of the area of the adjoining place of sampling. The Chauvigny site and the related quarry are located within the Vienne River valley. The outcrop and quarry, formed during the Jurassic period, rests in a depression between two Variscan structural highs: The Armorican Massif and the French Massif Central (Figure 5).

The tectonic patterns and kinematic characteristics of the Dogger formation are poorly understood. However, the typical underlying structural grain recognized in both the Southern Armorican Massif and the north-western edge of the French Massif Central is the presence of dextral transcurrent strike-slip faults within the frame of the Southern Armorican Shear Zone (SASZ; Figure 5).

During Variscan times, the Armorican Massif underwent deformations related to a major continental collision between Gondwana and Laurussia [34]. These resulted in the development of large dextral shear zones, including the SASZ, whose occurrence has been traced to the north-western edge of the French Massif Central. The dextral strike-slip component of the displacement is widely recognized across the Middle-Late Paleozoic Europe along NW-SE- and W-E-striking subconcentric wrench faults, e.g., Biscay-Pyrenees, Northern and Southern Armorican, Bristol Channel-Bray-Vittel, and North Artois faults [35,36].

Numerous neotectonic paleostress reconstructions, analyses of focal mechanism of earthquakes, and borehole breakouts across the entire Paris basin suggest that this right-lateral deformation of NW-SE- and W-E-striking subconcentric wrench faults is still ongoing. Shear patterns within the SASZ of Variscan age were independently mapped by different authors [37,38]. However, microseismical data showed that the SASZ is still a geodynamically active zone clearly pronounced in geomorphic patterns extracted from satellite imagery [39].



**Figure 5.** Geological map of the Paris Basin modified from the geological map of FRANCE (BRGM: Bureau de Recherches Géologiques et Minières—French geological survey) [33]. The rectangle with a dashed border shows the location of the frame of digital elevation model (DEM) for the Vienne Department region being used for the analysis of morpholineaments represented on Figures 6 and 7. SASZ—South Armorican dextral shear zone; BSZ—Bray dextral shear zone; NASZ—North Artois dextral shear zone. The white star marks the position of the Chauvigny quarry.

Gunzburger and Magnenet [40] used the up-to-date extensive synthesis of a huge database of outstandingly dense stress measurements in the Paris Basin obtained by ANDRA (the French radioactive waste management agency) in the framework of the feasibility study of underground nuclear waste storage. They confirmed that, on average, the major horizontal stress,  $\sigma_1$ , in the sedimentary cover of the basin has a constant NW–SE orientation, which is similar to the orientation of  $\sigma_1$ , generally accepted in the underlying basement. This means that Jurassic sediments overlying the Southern Armorican Shear Zone (SASZ) must be affected by this right lateral strike-slip faulting here. One of the possible methods to determine the proper spatial position studied in MIRAGES-2 device samples and fracture networks is to study these issues over the terrain overseen by the entire Vienne Department.

There is considerable evidence [41] that river valleys or, broadly speaking, ravine-gully networks follow tectonic structures, which are, to a large extent, determined by neotectonic processes and the related stress-field. This geomorphic phenomenon of neotectonically-controlled drainage networks is closely related to selective erosion process within zones of structural weakness.

A number of researchers [41,42] have used similarities between morpholineaments extracted from drainage patterns and mapped joint-fault distribution for identifying structural trends and delineating structure that have are buried, deep-seated, or masked by younger sediments. Analysis of digital models of land surface and river valleys, and ravine-gully networks by means of numerical geomorphology, provides a basis for recognizing faults and understanding their mutual arrangement and kinematic types. According to Scheidegger [41], joints controlling drainage networks and river valleys fragments are of tensile and shear origin and can be used as an effective instrument to reconstruct the neotectonic stress field.

So, to find a solution with azimuthal referencing of revealed fractures in the Lavoux samples, we decided (1) to delineate morpholineaments based on analysis of digital elevation models (DEM) of the land surface and (2) to perform spatial analysis of drainage patterns.

Figure 6 exhibits the shaded-relief elevation and drainage patterns in the Vienne Department area. Yellow dashed lines within Figure 6b correspond to morpholineaments extracted from a shaded-relief elevation visualization model. The lineaments visible here show the primary WNW–ESE orientation trending the SASZ as well as the lineations of subsidiary submeridional and sublatitudinal faults that appeared because of the dextral reactivation of the shear zone. However, the most spectacular evidence of right lateral reactivation of the SASZ and identification of trends of the principal and subsidiary fault systems is the fact that its formation can be derived from an analysis of drainage network patterns.

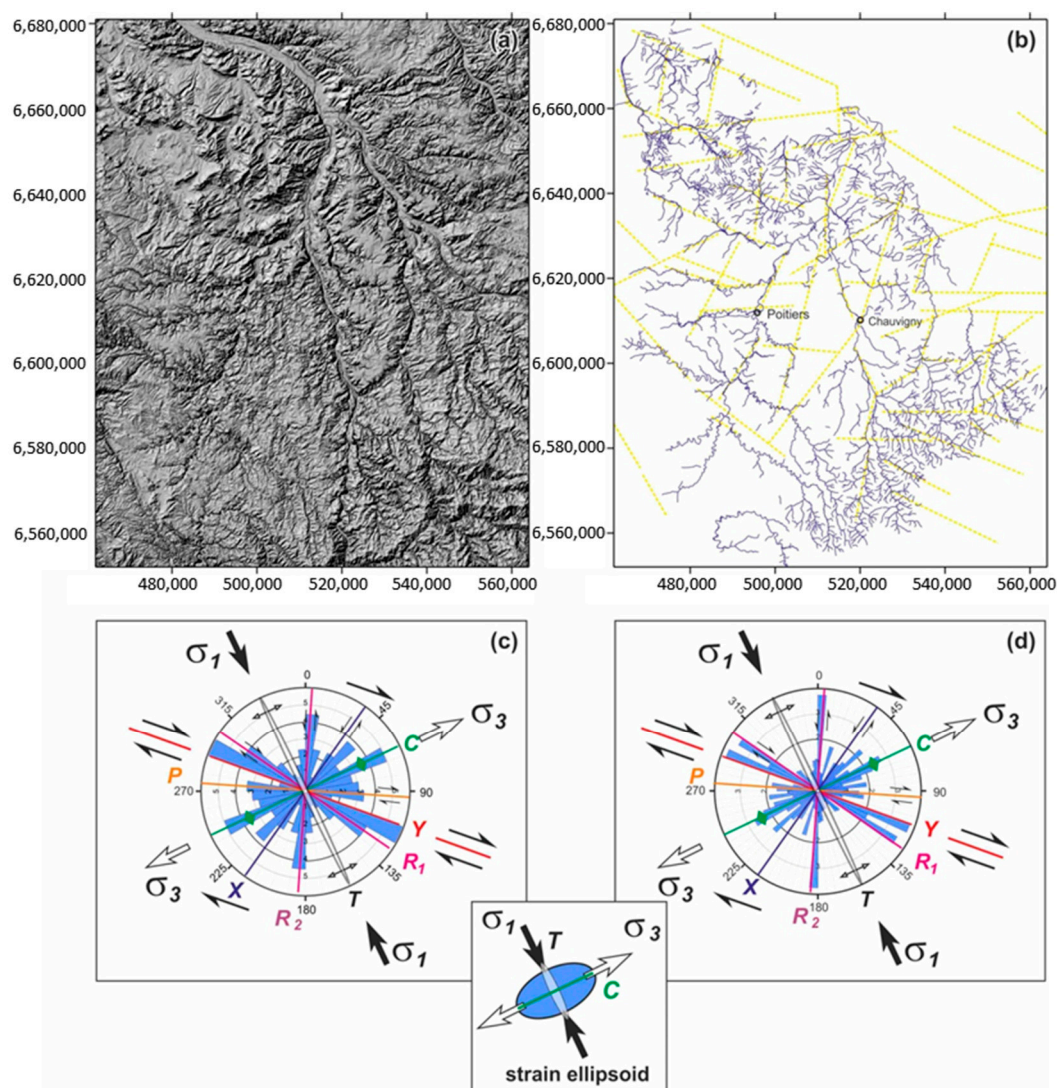


**Figure 6.** (a) Shaded-relief elevation and (b) drainage patterns in the area of the Vienne Department. (c,d) show drainage segment orientations in the rose diagrams with differentially assigned petal widths (10° and 5°, respectively). (b) Yellow dashed lines correspond to morpholineaments extracted from a shaded-relief elevation visualization model. The lowermost detail demonstrates a neotectonic strain ellipsoid orientation responsible for the formation of the recent drainage network.

Results of this analysis are presented in Figure 6c,d as drainage segment orientations in rose diagrams with differentially assigned petal widths (10° and 5°, respectively). The major petal

anomalies within the constructed rose diagrams are critically dependent on the main neotectonic stresses directions and the strain ellipsoid.

Both the most frequent drainage WNW–ESE-orientated lineations in Figure 6d coincide with the striking domain of the main dextral Y-shears and dextral  $R_1$ -shears. The angle between the bulk shear-zone boundary (or Y-shears) and  $R_1$ -shears is  $\sim 15^\circ$ , which corresponds to a  $\varphi/2$  ratio [27], where  $\varphi = 30 \pm 2^\circ$  is the internal friction angle of the host rock (Lavoux limestone) involved in strike-slip deformations.

Other drainage segment orientation extremes within the study area reflect submeridional NNE–SSW striking  $R_2$  sinistral shears, ENE–WSW striking compressional structures C (stylolitic planes within reversed faults and related compressional fold structures), dextral sublatitudinal P-shears, and sinistral X-shears.

The strike of principal shear zone Y (azimuth  $105\text{--}110^\circ$ ) and internal arrangement of subsidiary structures:  $R_1$  (azimuth  $120\text{--}125^\circ$ ),  $R_2$  (azimuth  $0\text{--}5^\circ$ ), C (azimuth  $60\text{--}65^\circ$ ), P (azimuth  $90\text{--}95^\circ$ ), and X (azimuth  $30\text{--}35^\circ$ ), are consistent with the strain ellipsoid where the principal compression stress ( $\sigma_1$ ) is  $150\text{--}155^\circ$ , with trending and extension stress ( $\sigma_3$ ) of  $60\text{--}65^\circ$ . Both principal stresses ( $\sigma_1$  and  $\sigma_3$ ) are lying sub-horizontally in the strike-slip stress regime.

Actually, the Vienne River's deflecting and meandering pattern (Figure 7a) can be represented by a combination of segments of a set of faults developed due to the right lateral reactivation of the SASZ.

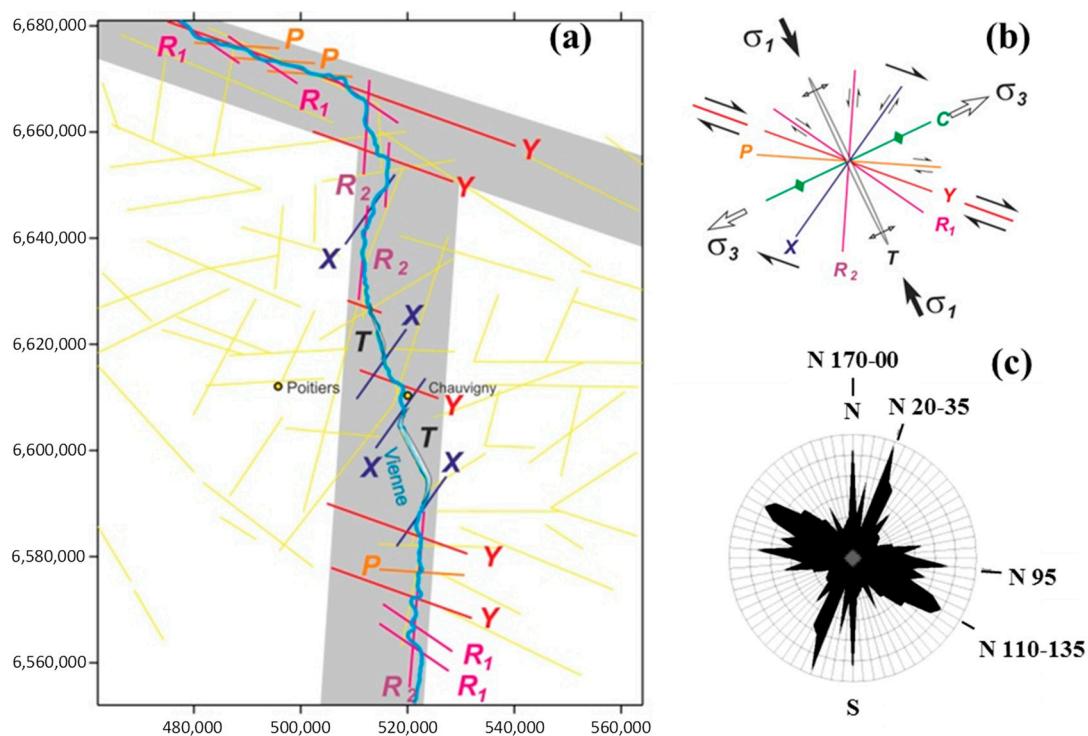


**Figure 7.** (a) Representation of major and minor trends of the Vienne River valley (shown by the blue line) derived from topography DEM as a combination of  $105\text{--}110^\circ$ , trending master shears Y, complimentary shears of  $R_1$  (azimuth  $120\text{--}125^\circ$ ), P (azimuth  $90\text{--}95^\circ$ ),  $R_2$  (azimuth  $0\text{--}5^\circ$ ), X (azimuth  $30\text{--}35^\circ$ ) types, and  $150\text{--}155^\circ$ , trending extensional joints T in a lazy S-shape. We inferred from the analysis of drainage patterns in the Vienne Department the azimuth of  $\sigma_1$ , the maximum principal stress in the strike-slip regime, is about  $N150\text{--}155^\circ$  E. Yellow dashed lines represent morpholineaments extracted from the shaded-relief elevation visualization model (Figure 6b). Grey zones correspond to two major directional clusters of the Vienne River valley represented by the master Y shears and secondary antithetic  $R_2$  shears. (b) Fractures orientation from this study. (c) Fractures identification from the Poitou threshold [43].

All major trends of the Vienne river valley seen in the topography DEM are represented by two major clusters corresponding to master Y shear and secondary  $R_2$  shear directions. However, the entrenched river's meanders appear to be composed of a number of differently-oriented straight segments controlled by fractures (lineaments). Streams follow these lineaments represented by master shears Y and complimentary shears of  $R_1$ , P,  $R_2$ , and X types, as well as dilatational fractures, T.

In accordance with Cornet and Röckel [44], the statistical distribution of the tension fracture orientations, identified within both the Dogger and the Oxfordian limestones of the Paris basin, exhibits a strong preferential orientation in the N150–155° E direction, i.e., parallel to the maximum horizontal stress direction developed during the Alpine tectonic orogeny.

The trend of extensional fissures, T (azimuth 150–155°), is relatively weakly expressed in the rose diagram for the entire drainage pattern of the study region. However, it becomes important for the Vienne River in the area just south and north of Chauvigny and seems to be morphologically and rheologically related to the outcropping, which is a relatively narrow strip of brittle Lavoux limestone. The characteristic lazy S-shape of the dilatational fracture, T, was created by the right lateral faulting along the set of master Y-shears, whose strikes correspond to the direction of the SASZ. We inferred from the analysis of drainage patterns in the Vienne department (Figures 6 and 7) the azimuth of  $\sigma_1$ , the maximum principal stress, is about N150–155° E.

These results are in good agreement with the general features of neotectonic stress reconstructions for the Poitou threshold and adjoining massifs summarized in previous publications (Figure 7c) [43–45]. Thermal remote sensing data allowed us to define the relation between fracturing and basement cover. Several observation studies of the outcrops of the Jurassic limestone defined the main directions of the preferential fractures (linked to the tectonic of the region). The cumulative rose diagram presented in this study (Figure 7b) confirms that the topolineaments controlling the Vienne River valley geometrical pattern developed in concert with two families of regional fractures: (1) Y,  $R_1$ , and P shears and (2)  $R_2$  and X shears. The slight maximum corresponding with tension fractures T is visible on this rose diagram.

### 3.5. Deciphering Spatial Orientations of Preferential Propagation of Dissolution Arrays after Experiments

Since Lavoux limestone sampled in-situ were affected by regional strain within a crustal-scale shear zone, we assumed that our samples, even without being subjected to the action of a regional stress field after extraction from the quarry, bear strain scars, i.e., fractures that can control or at least affect the morphology of the wormhole network.

The mechanical anisotropy caused by regional tectonic stresses in samples before experimental treatment seems to be a plausible factor for deciphering the spatial orientations of preferential propagation of experimentally-obtained dissolution conduits. The identical initial microstructure of samples extracted from one bulk sample of Lavoux limestone provides a strong basis for meaningful comparison of results. The azimuthal referencing of dissolution arrays was performed via rotation of obtained horizontal CT scans to provide the best fit in terms of an alignment for discrete fragments of dissolution arrays (which revealed microcracks enlarged by a dissolution process) with the scheme of orientations of kinematically-defined and mutually-crosscutting fracture sets inferred from regional tectonic and geomorphic patterns analyses (Figures 6 and 7).

Azimuthally-referenced CT scans of dissolution arrays and principal wormhole morphology, derived from the results of a spatial comparison of the results of experiments #1, #2, #3, and #4 (Figure 8) strongly support the influence of a principal displacement zone corresponding with bulk shear displacement Y (azimuth 105–110°) on the studied samples' right lateral reactivation within the limits of the SASZ, which affected the Dogger Formation in the region of sampling Lavoux limestone (Chauvigny quarry).

A total set of subsidiary Riedel system structures identified within horizontal CT scans of fresh samples (Figure 3) and samples after experiments (discrete fragments of dominant wormhole and entire dissolution patterns) demonstrate a strain ellipsoid, where the principal compression stress

( $\sigma_1$ ) is 150–155° and extension stress ( $\sigma_3$ ) is 60–65°. Both principal stresses ( $\sigma_1$  and  $\sigma_3$ ) are lying sub-horizontally in the strike-slip stress regime.

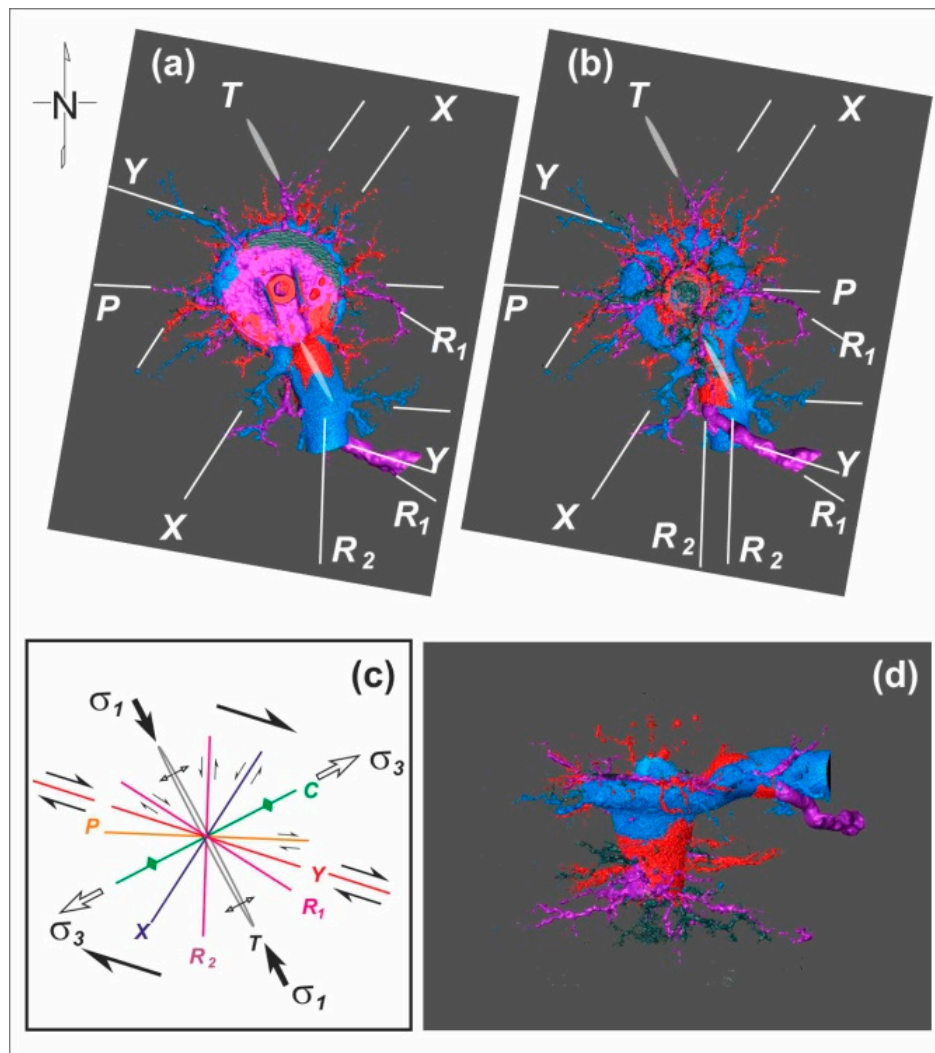


**Figure 8.** Azimuthally referenced structural control of dissolution arrays and principal wormhole morphology derived from the results of a spatial comparison of the experimental results: #1 (shown in grey), #2 (shown in purple), #3 (shown in red), #4 (shown in blue) in the framework of depicted orientations of fractures (c) appeared to be pronounced in the original sample of Lavoux limestones: (a) top view; (b) bottom vertically mirrored view; and (d) side 3D view.

#### 4. Discussion

The spatial geometry of progressively dissolving limestone media affected by CO<sub>2</sub>-rich solution injection into a well remains poorly understood. The most critical issue is the question about the morphology of the growing dissolution cavity, which could be theoretically represented by three possible scenarios.

The first scenario assumes mean dissolution rates in limestone with an appearance of a dissolution array of quasi-isometric shape that grew due to the stable dissolution front propagating in relatively homogeneous porous media. Here, mineral dissolution always occurs at the same distance from the injection point. The second scenario assumes an appearance of a dendritic dissolution pattern resulting from stochastic dissolution branching in porous limestone medium, where permeable regions have already inherited a pre-existing ramified pattern of chaotically connected macro-pores. The third

scenario supposes the highly channelized shape of dissolution arrays targeting fractures and zones of structural weakness. In radial flow, the last scenario provides a basis for considerable 3D variation in distances between the dissolution front and the injection point of the well. This variation might be subsequently eventualized in the trend in the dominating single principal wormhole as a potential leakage pathway from the injection well into adjoining stratigraphic intervals.

The results of our experimental studies, with the help of the MIRAGES-2 device, indicate the ground proof of the third scenario, where localized fast preferential fluid pathways are dependent on the pre-existing fracture network. We documented quick directional dissolution front propagation in the final scene of the dominant wormhole development in most cases of CO<sub>2</sub>-rich solution injection into core specimens, prominently pronounced even for relatively short time-driven experiments, #9 (12 h ageing, Figure 9) and #6 (24 h ageing, Figure 10).

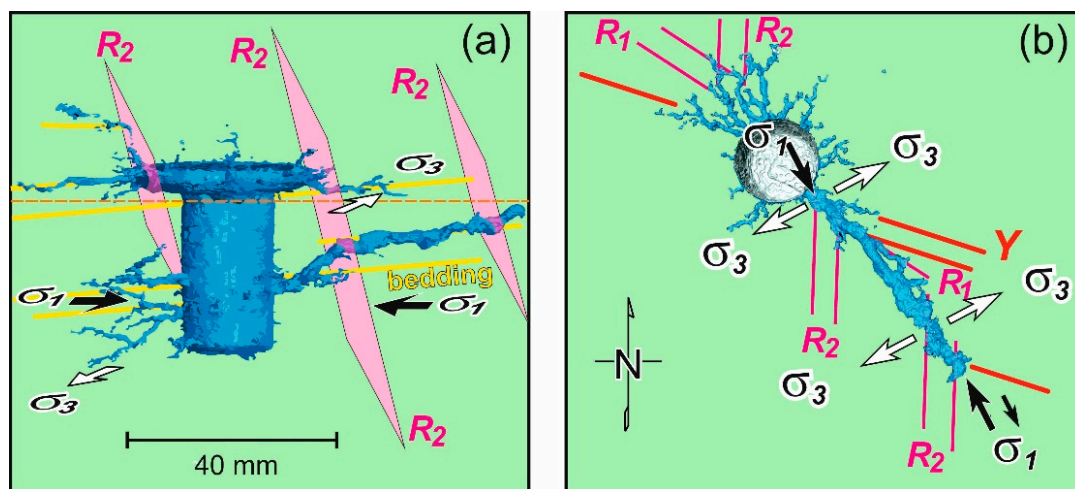


**Figure 9.** Results of structural interpretation of dissolution network/wormhole morphology for experiment #9 (12 h of CO<sub>2</sub>-rich solution injection into sample): (a) 3D model and (b) top view of the 3D model after CT inspection, horizontally cut at the level of the orange dashed line within inset (a).

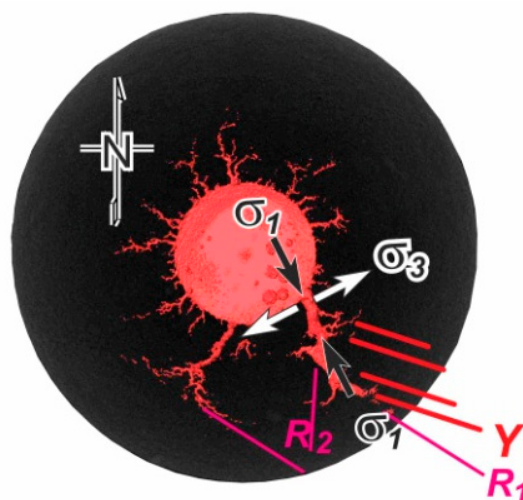


**Figure 10.** Results of structural interpretation of the dissolution network/wormhole morphology for experiment #6 (24 h CO<sub>2</sub>-rich solution injection into the sample).

Additional information about the distribution of dissolution networks and azimuthally referenced wormholing morphology trends were experimentally revealed after structurally interpreting the results of experiment #7 (Figure 11). From a technical point of view, experiment #7, with a core plug drilled at 55°, seems to be important because it was performed to mimic the real inclination of a pilot project

injection well. The results of 2D and 3D delineating of the dominant wormhole (Figure 11) indicate the non-horizontal saltatory mechanism of its propagation inside the core specimen. The spatial trend of the wormhole was governed by the interplay of both distributions, including the fracture systems with dramatically variable conductivity, which might serve as regions of attractors or obstacles for dissolution pathways, and intra-stratification (bedding) elements within the entire sample structure.

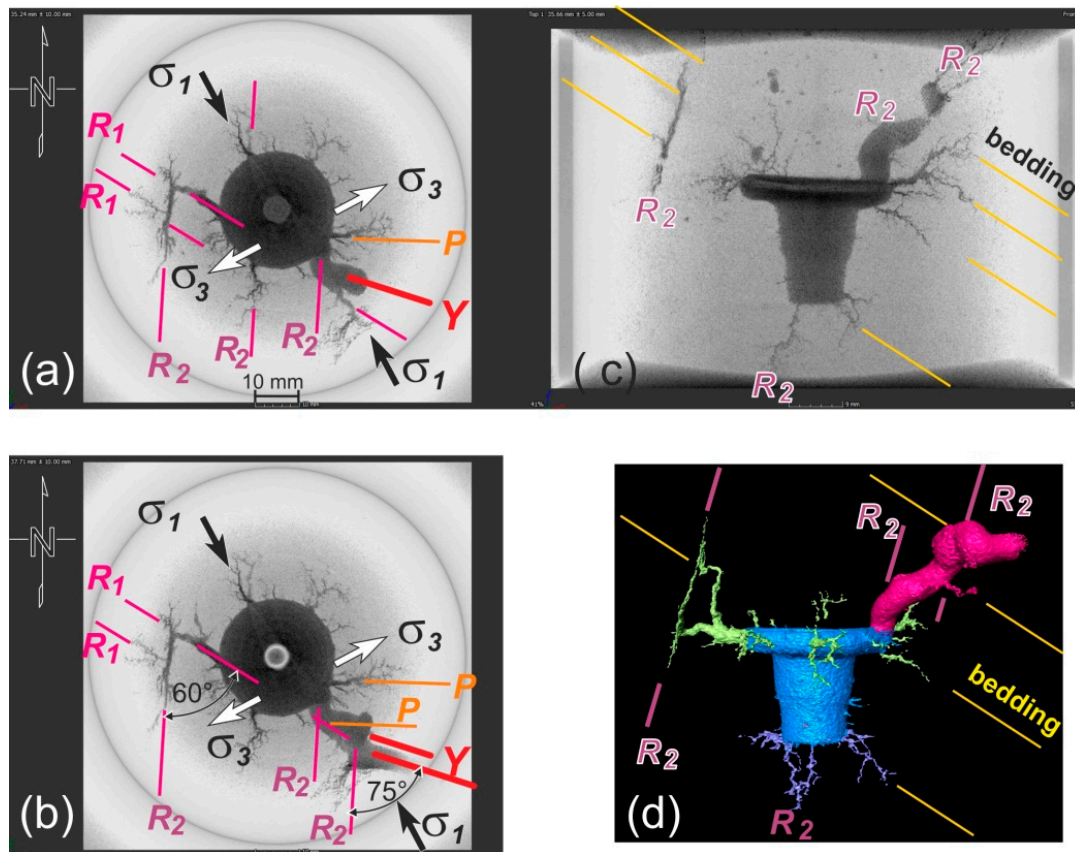


**Figure 11.** Results of structural interpretation of the dissolution network/wormhole morphology for experiment #7 (10 days of  $\text{CO}_2$ -rich solution injection into the sample drilled with inclination imitating injection well): (a) Horizontal CT scans showing progressive development of the principal wormhole from the level closed to the injection point (b) to the level closed to the top of cylindrical sample, (c) vertical CT scan in the E–W direction, and (d) 3D model showing the principal wormhole in pink.

So, on horizontal CT scans obtained of the dissolution mosaic (Figure 11a,b), it is shown that conjugated Riedel shears,  $R_1$  and  $R_2$ , intersected with one another and produced typical zones of strike-slip deformations with a rhombic block pattern. A model of experimental observations was reported with the angle of radial separation of discrete wormhole precursors  $60^\circ$  from each other under radial flow wormholing [46], which accommodates the effects of permeability anisotropy caused by natural fracturing.

From our point of view, this angle reflects the angle between the conjugated Riedel shears,  $60^\circ = 90^\circ - \varphi$  [27], where  $\varphi = 30 \pm 2^\circ$  is the internal friction angle of the host rock (Lavoux limestone) involved in strike-slip deformations. Notably, in some cases, the rhombic pattern of dissolution consists of fragments of master dextral Y-shears and antithetic sinistral  $R_2$  shears, intersecting each other at an angle of about  $75^\circ = 90^\circ - \varphi/2$  [27] (Figure 11a,b).

The initial strike of the observed mesoscopic wormholes appears to be NNW–SSE, trending parallel to dilatational fractures T (azimuth  $150$ – $155^\circ$ ), with a subsequent change in the major trends

of dissolution along the master Y shears (azimuth 105–110°) or, more specifically, including the combination of synthetic  $R_1$  shears and secondary synthetic P shears.

Practically, the same trend governing the wormhole strike is depicted in the rose diagram of the skeleton model constructed for the principal wormhole developed during experiment #7 (Figure 12).

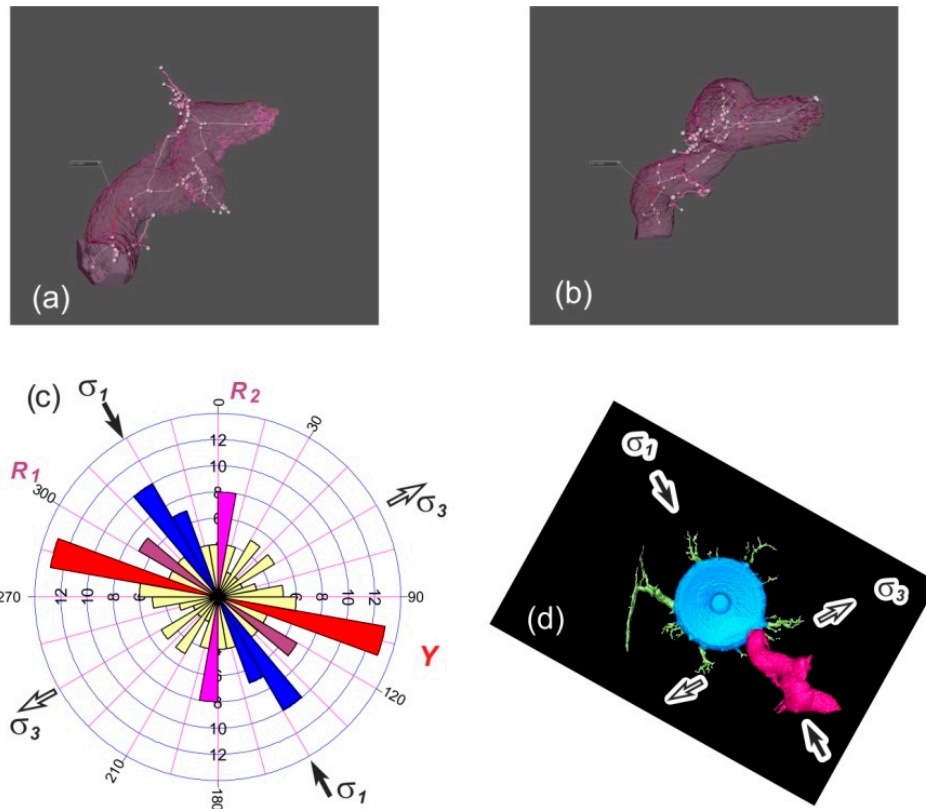


**Figure 12.** Skeleton model from CT 3D visualization of the principal wormhole represented as the (a) bottom and (b) vertical view of experiment #7. (c) Rose-diagram depicting the preferential directions of the growing principal wormhole, (d) which is shown in pink in the top view of the 3D model.

The revealed antithetic  $R_2$  shears served as obstacles for dissolution pathways, creating conditions for “jumping” a wormhole from one level to another elevated level (Figures 9–12).

Microstructural analysis of the studied sample (experiment #7) via binary filtration of high-resolution photographs of the  $R_2$  fracture wall demonstrated that this antithetic Riedel shear organizes itself as a rough indented surface due to the presence of slickolitic teeth oblique to the surface of shear displacement (Figure 13).

At this millimeter scale, small conic dissolution pits are visible parallel to the maximum compressive stress,  $\sigma_1$ .

Additional proof of the presence of conically shaped localized slickolitic teeth was derived for the same wall at the micron scale with the help of Scanned Electronic Microscope (SEM) image analysis. The teeth inclined to the wall of the fracture fossilized signatures of the stress field clearly indicate the strike-slip kinematic type of this fracture (Figure 14).



**Figure 13.** Correlation of results obtained with help of the CT 3D model in (a) the W–E direction and (b) microstructural analysis of a high-resolution photo of the vertical section of the studied sample for experiment #7 with outcrop scale structural patterns in the quarry excavating the Lavoux limestones. Note, the elements of the roughness for the slickolitic surface of  $R_2$  shears affected the dissolution pathways and geometric shape of the principal wormhole, shown in pink in the inset in (a).

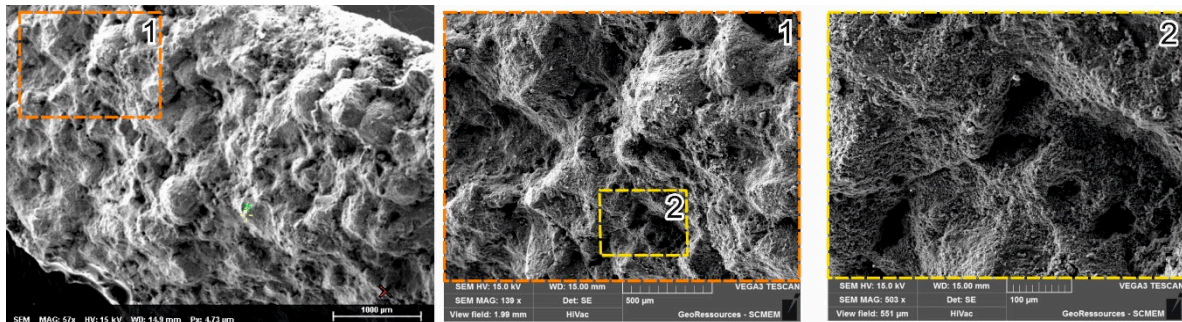


**Figure 14.** Multiscale Scanned Electronic Microscope (SEM) details of conical slickolites within the wall of the  $R_2$  shear within the studied sample (experiment #7).

The microslickolitic topography (combination of dissolution picks and pits) demonstrates the similar behavior over a range of scales studied. From our point of view, this serves as the main reason for generating both in-situ significant roughness and a related drop in conductivity within domains of the antithetic  $R_2$  shears. This feature can be illustrated by calculating the 3D distribution of the mean curvature,  $H$ , for the surfaces of the dominant wormhole and subsidiary dissolution arrays extracted from CT images for experiment #7 with following 3D visualization using Avizo software. In mathematics, the mean curvature,  $H$ , of a surface,  $S$ , is a measure of the surface deviation from a flat plane. First, a surface ( $S$ ), as a triangular approximation of the extrinsically segmented volumes of the entire dissolution pattern, was created. Second, the mean curvature ( $H$ ) was calculated using the formula:

$$H = (k_1 + k_2)/2, \tag{1}$$

where  $k_1$  and  $k_2$  are the principal curvatures of the curves resulting from the intersection between the surface,  $S$ , and orthogonal planes containing the normal vectors.

An invariant under rotation, the principal curvatures were calculated considering direct neighbours to a certain triangle of the surface.

The constructed 3D model of the mean curvature distribution (Figure 15a) indicates that highly curved (shown in red), and highly indented rough regions of the surface,  $S$ , strongly gravitated to domains of  $R_2$  shears, with partial propagation along bedding surfaces. Note the prominent positive anomaly of the mean curvature recorded within the node of intersection of the principal wormhole with the  $R_2$  fracture plane (Figure 15b), which acted as an impermeable barrier. Here, a fluid flow touched the steep dipping fracture seal, providing the hopping extension of the dominant wormhole into the upper levels, where tectonically-induced preferential direction facilitated its further growth. Irrespective of the precise mechanism controlling surface reactivity, our results indicate that, beyond the  $R_2$  fracture domain, the surface of the wormhole is almost polished, which is why it is characterized by minimal values of the mean curvature (shown in blue).

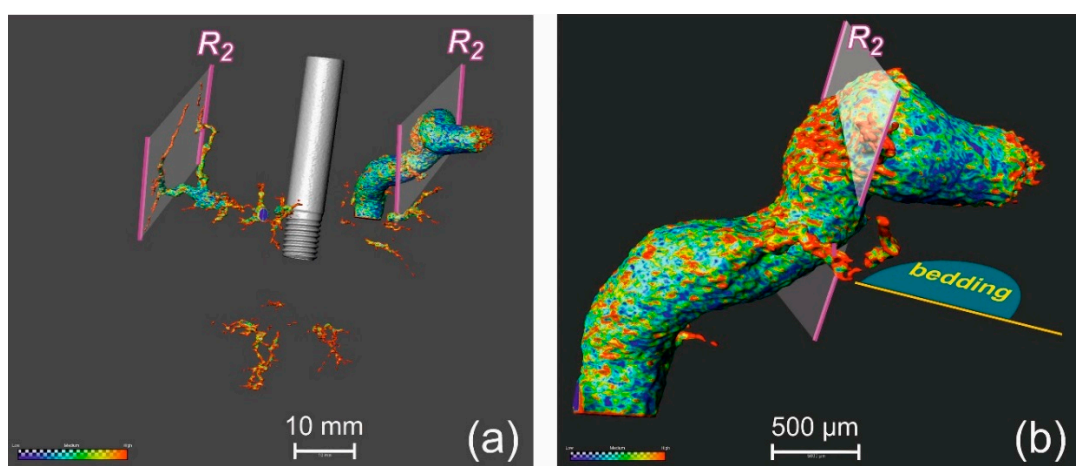


**Figure 15.** 3D model of the mean curvature distribution,  $H$ , for (a) the entire dissolution pattern and (b) the principal wormhole. Maximally and minimally curved areas are shown in red and in blue, respectively.

A question can be raised concerning the difference in conductivity for conjugated  $R_1$  and  $R_2$  shears. Instead of the classical theory of failure mechanics predicting equitable growth of two sets of Riedel shears, physical experiments and field observations in granular rocks [47] suggest that  $R_1$  shears developed much better than  $R_2$  shears. In most of the studied cases, shear failure within the strike-slip zone starts with the primary development of a set of  $R_1$  fractures. Continuous, but narrow, zones of  $R_1$  structures are composed of individual shear fractures,  $R_1$ , linked by transfer zones containing en-echelon arranged dilatational jogs—tensile joints and normal faults, T [48,49]. Closely spaced, but relatively short,  $R_2$  fractures develop later due to secondary restraining in the spatially overlapping bridges between the already developed  $R_1$  fractures [47]. Therefore,  $R_2$  fractures are usually more subjected to local stress concentration and can be interpreted as a combination of tight shears and compressive jogs (micro-thrusts) serving as damper valves for sub-horizontal fluid conduction.

This point of view explains the multiscale asperity of surfaces for the antithetic  $R_2$  shears caused by the presence of tectonically-induced slickolitic peaks and pits, which may constitute fluid-flow barriers due to their different mineralogy, thus affecting the permeability distribution—wormhole growth geometry induced by  $\text{CO}_2$ -rich fluids.

Preliminary chemical analyses of Lavoux limestone within fragments of slickolitic surface of  $R_2$  shear and beyond by means of SEM TESCAN VEGA3, equipped with an N EDS detector, revealed a discrepancy in the chemical concentration of Si (1.34–2.76%), Al (1.17–2.55%), and Mg (0.24–0.59%), which were pronounced only within the  $R_2$  shear wall. The concentration of those elements beyond the fracture of the  $R_2$  shear type were almost zero.

This result supports the concept of dropping reactivity rates in experimental limestone core-plugs along the slickolitic surfaces of  $R_2$  shears. These fracture surfaces are affected by residual insoluble minerals that have already precipitated during the tectonically-driven dissolution of calcite.

Little is known about the growth process of cavities induced by aggressive fluid treatments in Lavoux limestones, especially in terms of their spatial position and morphology throughout subsequent dissolution phases. However, formation of an initial dissolution pathway parallel to the maximal compressive stress,  $\sigma_1$ , or in the direction of least resistance, is not surprising when considering the analogical influence of local stresses on the spatial control of opening magma-chamber ruptures and dyke injecting [50]. Hydraulic fractures in fracking technology are of tensile origin and in-situ stress predetermines their orientation. Their propagation trends parallel to the maximum horizontal stress,  $\sigma_1$  [51]. During underground mining activity in a burst-prone coal seam, the primary elongated rock-and-gas outburst cavity is also oriented in the direction of the  $\sigma_1$  axis [52].

## 5. Conclusions

Numerous experimental core injecting flow tests have documented the formation of highly conductive cylindrically channelized carbonate matrix acidizing, which may result in wormholing as rapid and mostly complete tunnelling within host rocks.

This study highlights the phenomenon of the structural control of the propagation of the dissolution network, as shown by the correlation between the direction of the different wormholes and the main regional stress field. The interplay of intra-stratification, fracture systems, and their kinematical environment largely controls the dissolution pattern induced by  $\text{CO}_2$ -rich fluids.

The formation of a primary dissolution pathway tends to start along a tensile fracture, T, with subsequent growth of the artificial cavity (wormhole), controlled by the existing network of fractures. The most prominent artificial “karstification” arrays propagate in volumes affected by master Y shears, synthetic  $R_1$  shears, and antithetic  $R_2$  shears.

Antithetic shears,  $R_2$ , organize themselves as slickolitic surfaces, which may act as fluid-flow barriers due to their different mineralogy, thus affecting the permeability distribution—wormhole growth geometry induced by  $\text{CO}_2$ -saturated solutions.

As an important and reasonable tool to document the spatial control of limestone surface reactivity and wormholing propagation, we propose using 3D mapping of the mean curvature of the dissolution array.

We conclude that inferred tectonically-triggered control of the initiation and subsequent evolution of the dissolution pattern create possibilities for the implementation of industrial CCS projects because our results seriously reduce the spatial and morphologic uncertainties in characteristic shapes for growing dissolution structures.

**Author Contributions:** Conceptualization, V.P., A.R., J.S. and J.P.; Data curation, C.M.; Formal analysis, V.P. and C.M.; Funding acquisition, J.S.; Investigation, A.R.; Project administration, A.R., J.R. and J.P.; Software, C.M.; Supervision, J.P.; Writing—original draft, V.P., A.R. and J.R.

**Funding:** This work was supported and financed by the Scientific Interest Group Geodenergies through the PILOTE  $\text{CO}_2$ -DISSOLVED project (ANR-10-IEED-0804 PILOTE  $\text{CO}_2$  DISSOLVED).

**Acknowledgments:** The authors would like to acknowledge Maxime Dargent for technical assistance in SEM analyses. Our acknowledgements go to Robert Rainbird (Natural Resources Canada and Geological Survey of Canada) for fruitful comments and significant improvement of English text.

**Conflicts of Interest:** The authors declare no conflict of interest. The founding sponsors had no role in the design of the study; in the collection, analyses, or interpretation of data; in the writing of the manuscript; or in the decision to publish the results.

## References

1. Grataloup, S.; Bonijoly, D.; Brosse, E.; Dreux, R.; Garcia, D.; Hasanov, V.; Lescanne, M.; Renoux, P.; Thoraval, A. A site selection methodology for CO<sub>2</sub> underground storage in deep saline aquifers: Case of the Paris Basin. *Energy Procedia* **2009**, *1*, 2929–2936. [[CrossRef](#)]
2. Brosse, E.; Badinier, G.; Blanchard, F.; Caspard, E.; Collin, P.Y.; Delmas, J.; Dezayes, C.; Dreux, R.; Dufournet, A.; Durst, P.; et al. Selection and Characterization of Geological Sites able to Host a Pilot-Scale CO<sub>2</sub> Storage in the Paris Basin (GéoCarbone-PICOREF). *Oil Gas Sci. Technol. Rev. IFP* **2010**, *65*, 375–403. [[CrossRef](#)]
3. Le Guen, Y.; Renard, F.; Hellmann, R.; Brosse, E.; Collombet, M.; Tisserand, D.; Gratier, J.P. Enhanced deformation of limestone and sandstone in the presence of high fluids. *J. Geophys. Res. Solid Earth* **2007**, *112*. [[CrossRef](#)]
4. Sterpenich, J.; Sausse, J.; Pironon, J.; Géhin, A.; Hubert, G.; Perfetti, E.; Grgic, D. Experimental ageing of oolitic limestones under CO<sub>2</sub> storage conditions: Petrographical and chemical evidence. *Chem. Geol.* **2009**, *265*, 99–112. [[CrossRef](#)]
5. Jobard, E.; Sterpenich, J.; Pironon, J.; Corvisier, J.; Jouanny, M.; Randi, A. Experimental simulation of the impact of a thermal gradient during geological sequestration of CO<sub>2</sub>: The COTAGES experiment. *Int. J. Greenh. Gas Control* **2013**, *12*, 56–71. [[CrossRef](#)]
6. Rahbari, S.H.E.; Saberi, A.A. Attracted diffusion-limited aggregation. *Phys. Rev. E* **2012**, *86*, 011407. [[CrossRef](#)] [[PubMed](#)]
7. Fischer, C.; Lüttge, A. Beyond the conventional understanding of water–rock reactivity. *Earth Planet. Sci. Lett.* **2017**, *457*, 100–105. [[CrossRef](#)]
8. Lüttge, A.; Arvidson, R.S.; Fischer, C. Fundamental Controls of Dissolution Rate Spectra: Comparisons of Model and Experimental Results. *Procedia Earth Planet. Sci.* **2013**, *7*, 537–540. [[CrossRef](#)]
9. Kervévan, C.; Beddelem, M.-H.; O’Neil, K. CO<sub>2</sub>-DISSOLVED: A Novel Concept Coupling Geological Storage of Dissolved CO<sub>2</sub> and Geothermal Heat Recovery—Part 1: Assessment of the Integration of an Innovative Low-cost, Water-based CO<sub>2</sub> Capture Technology. *Energy Procedia* **2014**, *63*, 4508–4518. [[CrossRef](#)]
10. Kervévan, C.; Beddelem, M.-H.; Galiègue, X.; Le Gallo, Y.; May, F.; O’Neil, K.; Sterpenich, J. Main Results of the CO<sub>2</sub>-DISSOLVED Project: First Step toward a Future Industrial Pilot Combining Geological Storage of Dissolved CO<sub>2</sub> and Geothermal Heat Recovery. *Energy Procedia* **2017**, *114*, 4086–4098. [[CrossRef](#)]
11. Sterpenich, J.; Jobard, E.; El Hajj, H.; Pironon, J.; Randi, A.; Caumon, M.-C. Experimental study of CO<sub>2</sub> injection in a simulated injection well: The MIRAGES experiment. *Greenh. Gases Sci. Technol.* **2013**, *4*, 210–224. [[CrossRef](#)]
12. Randi, A.; Sterpenich, J.; Morlot, C.; Pironon, J.; Kervévan, C.; Beddelem, M.H.; Fléhoc, C. CO<sub>2</sub>-DISSOLVED: A Novel Concept Coupling Geological Storage of Dissolved CO<sub>2</sub> and Geothermal Heat Recovery—Part 3: Design of the MIRAGES-2 Experimental Device Dedicated to the Study of the Geochemical Water-Rock Interactions Triggered by CO<sub>2</sub> Laden Brine Injection. *Energy Procedia* **2014**, *63*, 4536–4547. [[CrossRef](#)]
13. Randi, A.; Sterpenich, J.; Thiéry, D.; Kervévan, C.; Pironon, J.; Morlot, C. Experimental and Numerical Simulation of the Injection of a CO<sub>2</sub> Saturated Solution in a Carbonate Reservoir: Application to the CO<sub>2</sub>-DISSOLVED Concept Combining CO<sub>2</sub> Geological Storage and Geothermal Heat Recovery. *Energy Procedia* **2017**, *114*, 2942–2956. [[CrossRef](#)]
14. Schechter, R.S.; Gidley, J.L. The change in pore size distribution from surface reactions in porous media. *AIChE J.* **2004**, *15*, 339–350. [[CrossRef](#)]
15. Daccord, G.; Lenormand, R. Fractal patterns from chemical dissolution. *Nature* **1987**, *325*, 41–43. [[CrossRef](#)]
16. Hoefner, M.L.; Fogler, H.S. Pore evolution and channel formation during flow and reaction in porous media. *AIChE J.* **2004**, *34*, 45–54. [[CrossRef](#)]
17. Gouze, P.; Noiriël, C.; Bruderer, C.; Loggia, D.; Leprovost, R. X-ray tomography characterization of fracture surfaces during dissolution. *Geophys. Res. Lett.* **2003**, *30*. [[CrossRef](#)]
18. Detwiler Russell, L. Permeability alteration due to mineral dissolution in partially saturated fractures. *J. Geophys. Res. Solid Earth* **2010**, *115*. [[CrossRef](#)]
19. Szymczak, P.; Ladd, A.J.C. Wormhole formation in dissolving fractures. *J. Geophys. Res. Solid Earth* **2009**, *114*. [[CrossRef](#)]

20. Gabrovšek, F.; Dreybrodt, W. A model of the early evolution of karst aquifers in limestone in the dimensions of length and depth. *J. Hydrol.* **2001**, *240*, 206–224. [[CrossRef](#)]
21. Ford, D.; Williams, P. Introduction to Karst. In *Karst Hydrogeology and Geomorphology*; Wiley-Blackwell: Hoboken, NJ, USA, 2013; pp. 1–8. ISBN 978-1-118-68498-6.
22. Ballesteros, D.; Jiménez-Sánchez, M.; García-Sansegunado, J.; Borreguero, M. SpeleoDisc: A 3D quantitative approach to define the structural control of endokarst: An application to deep cave systems from the Picos de Europa, Spain. *Geomorphology* **2014**, *216*, 141–156. [[CrossRef](#)]
23. Sauro, F.; Zampieri, D.; Filipponi, M. Development of a deep karst system within a transpressional structure of the Dolomites in north-east Italy. *Geomorphology* **2013**, *184*, 51–63. [[CrossRef](#)]
24. Collon, P.; Bernasconi, D.; Vuilleumier, C.; Renard, P. Statistical metrics for the characterization of karst network geometry and topology. *Geomorphology* **2017**, *283*, 122–142. [[CrossRef](#)]
25. Nijman, W.; Savage, J.F. Persistent basement wrenching as controlling mechanism of Variscan thin-skinned thrusting and sedimentation, Cantabrian Mountains Spain. *Tectonophysics* **1989**, *169*, 281–302. [[CrossRef](#)]
26. Garcia-Rios, M.; Luquot, L.; Soler, J.M.; Cama, J. Influence of the flow rate on dissolution and precipitation features during percolation of CO<sub>2</sub>-rich sulfate solutions through fractured limestone samples. *Chem. Geol.* **2015**, *414*, 95–108. [[CrossRef](#)]
27. Hancock, P.L. Brittle microtectonics: Principles and practice. *J. Struct. Geol.* **1985**, *7*, 437–457. [[CrossRef](#)]
28. Granier, B.; Staffelbach, C. Quick look cathodoluminescence analyses and their impact on the interpretation of carbonate reservoirs. Case study of mid-Jurassic oolitic reservoirs in the Paris Basin. *Carnets de Geologie* **2009**, G2009\_A07. [[CrossRef](#)]
29. Sylvester, A.G. Strike-Slip Faults. *GSA Bull.* **1988**, *100*, 1666–1703. [[CrossRef](#)]
30. Cariou, É.; Poncet, D.; Colchen, M.; Karnay, G.; Becqgiraudon, J.-F.; avec la collaboration de Branger, P.; Coirier, B.; Dubois, D.; Porel, G.; Thomassin, H. *Notice Explicative, Carte géol. France (1/50 000), feuille Saint-Maixent-l'École (611)*; BRGM: Orléans, France, 2006; 132p, ISBN 13: 978-2-7159-1611-1.
31. Scale invariance. In *Fractals and Chaos in Geology and Geophysics*; Turcotte, D.L. (Ed.) Cambridge University Press: Cambridge, UK, 1997; pp. 1–5. ISBN 978-0-521-56733-6.
32. Tchalenko, J.S. Similarities between Shear Zones of Different Magnitudes. *GSA Bull.* **1970**, *81*, 1625–1640. [[CrossRef](#)]
33. *Carte Géologique de la FRANCE: 1/1 000000*; BRGM: Orléans, France, 2003; ISBN 978-7-159-21586-8.
34. Ballèvre, M.; Bosse, V.; Ducassou, C.; Pitra, P. Palaeozoic history of the Armorican Massif: Models for the tectonic evolution of the suture zones. *Comptes Rendus Geosci.* **2009**, *341*, 174–201. [[CrossRef](#)]
35. Badham, J.P.N.; Halls, C. Microplate tectonics, oblique collisions, and evolution of the Hercynian orogenic systems. *Geology* **1975**, *3*, 373–376. [[CrossRef](#)]
36. Arthaud, F.; Matte, P. Late Paleozoic strike-slip faulting in southern Europe and northern Africa: Result of a right-lateral shear zone between the Appalachians and the Urals. *GSA Bull.* **1977**, *88*, 1305–1320. [[CrossRef](#)]
37. Jégouzo, P. The South Armorican Shear Zone. *J. Struct. Geol.* **1980**, *2*, 39–47. [[CrossRef](#)]
38. Rolin, P.; Marquer, D.; Colchen, M.; Thieblemont, D.; Rossi, P. Progressive shortening axis rotation recorded by Variscan synkinematic granites: Example of the South Armorican shear zone in the Vendée (France). *Geodinamica Acta* **2008**, *21*, 203–218. [[CrossRef](#)]
39. Yésou, H.; Rolet, J. Regional mapping of the South Armorican shear zone (Brittany, France) using remotely sensed SPOT imagery. *ISPRS J. Photogramm. Remote Sens.* **1990**, *45*, 419–427. [[CrossRef](#)]
40. Gunzburger, Y.; Magnenet, V. Stress inversion and basement-cover stress transmission across weak layers in the Paris basin, France. *Tectonophysics* **2014**, *617*, 44–57. [[CrossRef](#)]
41. Scheidegger, A.E. *Morphotectonics*; Springer: Berlin/Heidelberg, Germany, 2011; ISBN 978-3-642-18746-9.
42. Štěpánčíková, P.; Stemberk, J.; Vilímek, V.; Košťák, B. Neotectonic development of drainage networks in the East Sudeten Mountains and monitoring of recent fault displacements (Czech Republic). *Geomorphology* **2008**, *102*, 68–80. [[CrossRef](#)]
43. Burbaud-Vergneaud, M. *Fracturation et Interactions Socle Couverture: Le Seuil du Poitou [Fracturing and Interactions Crystalline Basement Overlays: The “Poitou threshold”]*. Ph.D. Thesis, University of Poitiers, Poitiers, France, 1987.
44. Cornet, F.H.; Röckel, T. Vertical stress profiles and the significance of “stress decoupling”. *Tectonophysics* **2012**, *581*, 193–205. [[CrossRef](#)]

45. Bourbiaux, B.; Callot, J.P.; Doligez, B.; Fleury, M.; Gaumet, F.; Guiton, M.; Lenormand, R.; Mari, J.-F.; Pourpak, F. Multi-Scale Characterization of an Heterogeneous Aquifer Through the Integration of Geological, Geophysical and Flow Data: A Case Study. *Oil Gas Sci. Technol. Rev. IFP* **2007**, *63*. [[CrossRef](#)]
46. Gdanski, R. A Fundamentally New Model of Acid Wormholing in Carbonates. In Proceedings of the SPE European Formation Damage Conference, The Hague, The Netherlands, 31 May–1 June 1999. SPE-54719-MS. [[CrossRef](#)]
47. Misra, S.; Mandal, N.; Chakraborty, C. Formation of Riedel shear fractures in granular materials: Findings from analogue shear experiments and theoretical analyses. *Tectonophysics* **2009**, *471*, 253–259. [[CrossRef](#)]
48. Goncharov, M.A.; Rogozhin, E.; Frolova, N.S.; Rozhin, P.N.; Zakharov, V. Riedel megashears R' and the trend to gravitational equilibrium as main factors of tsunamigenic earthquakes. *Geodinamika i Tektonofizika* **2014**, *5*, 939–991. [[CrossRef](#)]
49. Rao, G.; Lin, A.; Yan, B.; Jia, D.; Wu, X.; Ren, Z. Co-seismic Riedel shear structures produced by the 2010 Mw 6.9 Yushu earthquake, central Tibetan Plateau, China. *Tectonophysics* **2011**, *507*, 86–94. [[CrossRef](#)]
50. Gudmundsson, A. How local stresses control magma-chamber ruptures, dyke injections, and eruptions in composite volcanoes. *Earth-Sci. Rev.* **2006**, *79*, 1–31. [[CrossRef](#)]
51. Huang, J.; Griffiths, D.V.; Wong, S.-W. In situ stress determination from inversion of hydraulic fracturing data. *Int. J. Rock Mech. Min. Sci.* **2011**, *48*, 476–481. [[CrossRef](#)]
52. Sachsenhofer, R.F.; Privalov, V.A.; Panova, E.A. Basin evolution and coal geology of the Donets Basin (Ukraine, Russia): An overview. *Int. J. Coal Geol.* **2012**, *89*, 26–40. [[CrossRef](#)]



© 2019 by the authors. Licensee MDPI, Basel, Switzerland. This article is an open access article distributed under the terms and conditions of the Creative Commons Attribution (CC BY) license (<http://creativecommons.org/licenses/by/4.0/>).